Journal of Magnetic Resonance 212 (2011) 74–85

Contents lists available at ScienceDirect

Journal of Magnetic Resonance

journal homepage: www.elsevier.com/locate/jmr

Cardiac-induced physiological noise in 3D gradient echo brain imaging: Effect of *k*-space sampling scheme

Anders Kristoffersen *, Pål Erik Goa

MI Lab, Department of Medical Imaging, St. Olavs Hospital HF, N-7006 Trondheim, Norway

ARTICLE INFO

Article history:
Received 1 October 2010
Revised 14 June 2011
Available online 19 July 2011

Keywords:
3D acquisition
Physiological noise
Quasiperiodic oscillation
Compressed sensing
Signal-to-noise

ABSTRACT

The physiological noise in 3D image acquisition is shown to depend strongly on the sampling scheme. Five sampling schemes are considered: Linear, Centric, Segmented, Random and Tuned. Tuned acquisition means that data acquisition at *k*-space positions k and $-k$ are separated with a specific time interval. We model physiological noise as a periodic temporal oscillation with arbitrary spatial amplitude in the physical object and develop a general framework to describe how this is rendered in the reconstructed image. Reconstructed noise can be decomposed in one component that is in phase with the signal (parallel) and one that is 90° out of phase (orthogonal). Only the former has a significant influence on the magnitude of the signal. The study focuses on fMRI using 3D EPI. Each *k*-space plane is acquired in a single shot in a time much shorter than the period of the physiological noise. The above mentioned sampling schemes are applied in the slow *k*-space direction and noise propagates almost exclusively in this direction. The problem then, is effectively one-dimensional. Numerical simulations and analytical expressions are presented. 3D noise measurements and 2D measurements with high temporal resolution are conducted. The measurements are performed under breath-hold to isolate the effect of cardiac-induced pulsatile motion. We compare the time-course stability of the sampling schemes and the extent to which noise propagates from a localized source into other parts of the imaging volume. Tuned and Linear acquisitions perform better than Centric, Segmented and Random.

1. Introduction

3D *k*-space acquisition has a number of advantages over 2D. With large stacks the signal-to-noise ratio (SNR) is improved. The voxels are better defined than 2D voxels, which have a non-rectangular profile in the slice-select direction. Furthermore, a 3D isotropic data set can be reconstructed in arbitrary planes. 3D acquisition is used in 3D echo-planar imaging (EPI) [1,2], which is the main interest of the present paper, but also in steady-state free precession [3], and PRESTO [4]. Furthermore, it is popular in compressed sensing since the virtues of this technique increase with the dimensionality of the acquisition *k*-space [5].

In functional MRI, the total noise is often dominated by physiological rather than thermal noise [6,7]. The physiological noise level increases proportionally to the signal intensity [6]. Hence, the total SNR as a function of the thermal SNR approaches asymptotically a maximum attainable value.

The most prominent sources of physiological noise are breathing and cardiac-induced pulsatile motion that appear as quasiperiodic oscillations [8]. In addition, there are fluctuations in the resting brain with frequencies lower than 0.1 Hz [9]. This can be used to investigate brain connectivity, but appears as noise in paradigm-based functional imaging.

Respiration induces approximately global phase shifts that can be compensated with techniques such as correction of dynamic off-resonance in *k*-space [10] or real-time B_0 shimming [11]. Cardiac-induced pulsatile motion has local effects and is therefore more difficult to correct. This problem is the focus of the present paper.

Although physiological noise has been studied extensively for 2D acquisition [6,12–15], less is known about its effects in 3D. An important difference between 2D and 3D acquisition is that a single shot 2D slice can be read out in a time shorter than the typical period of the physiological noise, T_{phys}, which is approximately one second for cardiac-induced motion. This means that cardiac-induced noise can be reduced by band-stop filtering of the time series or by retrospective correction techniques [8,16]. Such techniques cannot be applied to a 3D cube, since it is usually read out in a period that includes several heart beats.

The origins and characteristics of cardiac-induced physiological noise signals with 2D EPI sampling have been investigated [17–19]. Effects on phase images have also been reported in other studies [20,21]. Important noise sources are pulsative contraction and expansion of ventricles and large blood vessels, pulsating cerebro-spinal fluid (CSF) flow and blood flow.

* Corresponding author. Fax: +47 72 57 57 69.
E-mail address: Anders.Kristoffersen@stolav.no (A. Kristoffersen).

1090-7807/$ - see front matter © 2011 Elsevier Inc. All rights reserved.
doi:10.1016/j.jmr.2011.06.012

The purpose of the present paper is to examine how the manifestations of cardiac-induced physiological noise with 3D acquisitions depend on the way k-space is traversed. This is something that, to our knowledge, has not been investigated previously. We analyze noise propagation for five sampling schemes. We define a model for periodic signals with arbitrary spatial amplitudes. This model is general and applicable to, but not limited to, physiological noise signals. The model is analyzed numerically and, in part, analytically. We also conduct human brain measurements that we interpret in light of the results of the mathematical analysis.

2. Theory

The sampling scheme is the way in which k-space is traversed. Fig. 1 shows five possibilities. We restrict the discussion to a one-dimensional model. This is adequate for 3D EPI-based sequences where a k-space plane is read out in a time much shorter than the period of the cardiac-induced physiological noise signal. Noise is then propagated mainly in the slowest k-space direction. In Fig. 1, each circle represents one plane in k-space.

2.1. Noise model

The amplitude of the cardiac-induced pulsatile motion has a strong spatial dependence. It is greatest in CSF and in the vicinity of the major vessels. The temporal oscillation is quasi-periodic. As a first order approximation, we assume perfect periodicity within the time interval required for the acquisition of one volume. With an exception for arrhythmic patients, this is reasonable when the volume time is not too long (typically a few seconds) compared to the period of the physiological noise (typically one second). The noise measurements described in the Results section justify a model with localized noise sources and periodic oscillations.

Mathematically, we model physiological noise as a periodic temporal oscillation with an amplitude that is given by an arbitrary spatial function, $h(z)$. The temporal oscillation is assumed to be independent of spatial position, i.e. the model is separable. The temporal oscillation is denoted $g(t)$ and satisfies the periodicity condition $g(t) = g(t + T_{\text{phys}})$. In the numerical model described in section Experimental setup, $h(z)$ is chosen as a Gaussian, that is, we consider a localized noise source.

The total signal, $s_{\text{total}}(z,t)$, is the sum of a static, underlying signal, $S(z)$, a time-dependent, physiological noise signal, $p(z,t)$, and white, thermal noise ε, i.e.

$$s_{\text{total}}(z,t) = S(z) + p(z,t) + \varepsilon. \tag{1}$$

The static signal consists of a magnitude part and a phase,

$$S(z) = M(z)\exp[i\varphi(z)]. \tag{2}$$

The phase depends on factors such as local magnetic field offset and bulk motion. The phase drift is usually small on the time scale set by the volume acquisition time, hence it is assumed to be a function of the position only. Unlike thermal noise, physiological noise is a part of the physical object that is being imaged. The factors that determine the phase for the static signal will therefore affect the physiological noise in a similar fashion. We hence assume that the phase $\varphi(z)$ is also present in the physiological noise. The full expression for the physiological noise is then

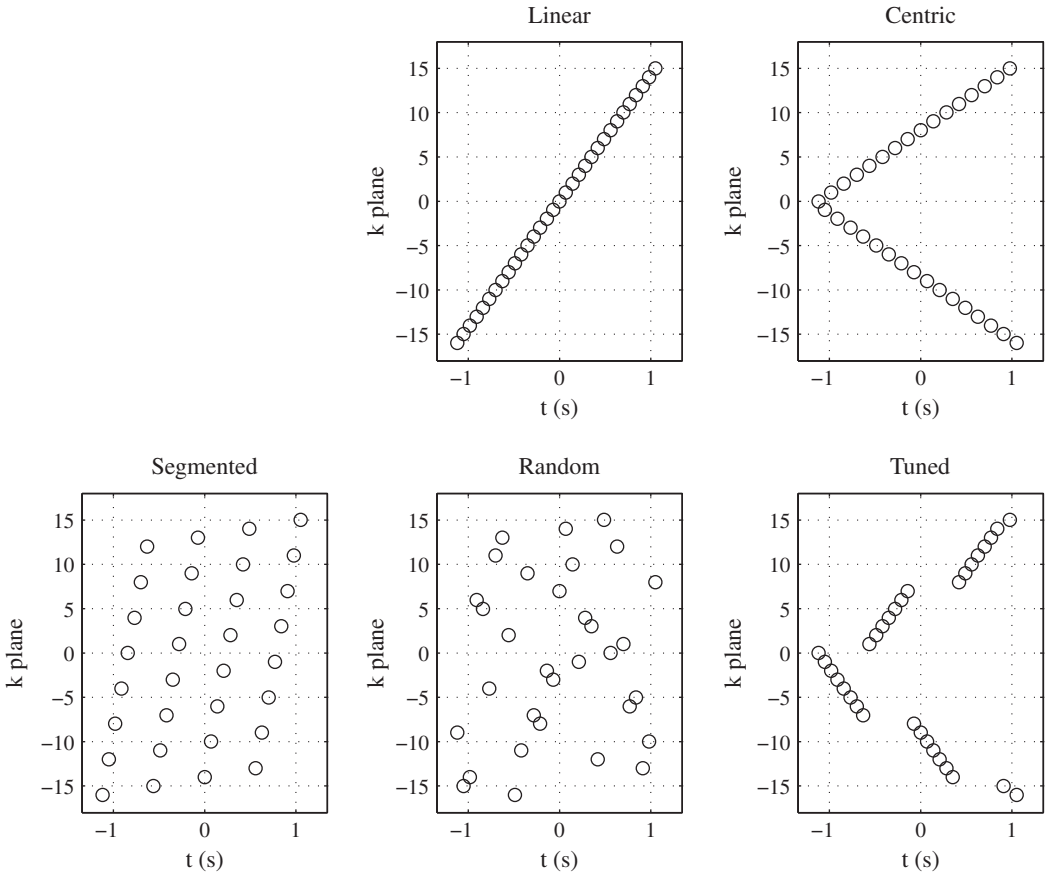

Fig. 1. Sampling schemes for a one-dimensional model with 32 k-space planes. The Segmented scheme is shown with $N_{\text{seg}} = 4$ segments. In terms of 3D acquisition, each circle represents one plane in k-space.

$$p(z,t,t_0) = \exp[i\varphi(z)]h(z)g(t-t_0), \tag{3}$$

where the offset t_0 in the temporal function will vary across consecutive volumes as a function of T_{phys} and the acquisition time for one volume, T_{vol}. The increase from one volume to the next is given by

$$\Delta t_0 = T_{\text{vol}} \bmod T_{\text{phys}}. \tag{4}$$

This equation assumes perfect periodicity. With quasiperiodic oscillations the evolution of t_0 will become less predictable. The spatial function $h(z)$ is real-valued by convention, whereas the temporal function $g(t)$ can be real, imaginary or complex. This depends on the nature of the physiological noise, which could be quasiperiodic pulsatile flow, tissue motion or periodic variations in the B_0 field (which induces phase variations). Since the Fourier transform is linear, each term in Eq. (1) can be treated separately. We shall be concerned with the physiological noise, Eq. (3).

The temporal oscillation in Eq. (3) can be decomposed in a Fourier series,

$$g(t) = \sum_{n=-\infty}^{\infty} G_n \exp\left(\frac{2\pi i n}{T_{\text{phys}}} t\right), \tag{5}$$

where G_n are the Fourier components. The DC component, G_0, is zero by construction since it can be included as a part of the background, static signal, $S(z)$. A simple special case is pure harmonic oscillation, where $G_n = 0$ for $|n| \geqslant 2$.

The k-space representation of the physiological noise at time t is given by the spatial Fourier transform of Eq. (3)

$$P(k,t,t_0) = \mathbf{F}\{\exp[i\varphi(z)]h(z)\}g(t-t_0), \tag{6}$$

where $\mathbf{F}$ denotes Fourier transformation (our Fourier convention is given in Appendix A). Note that the k-space function oscillates with the same period as the physiological noise signal. In a measurement, k-space is filled with samples taken at specific instants in time. This introduces a modulation of the measured k-space that depends on the sampling scheme. The position in k-space, k, is a function of the sampling time, t. The function $k(t)$ can be inverted to express t as a function of k, $t(k)$. This introduces a k dependence in the temporal function $g(t)$, Eq. (5). Combining Eqs. (5) and (6), we obtain a general expression for the sampled k-space representation of the physiological noise

$$P_S(k,t_0) = \mathbf{F}\{\exp[i\varphi(z)]h(z)\} \sum_{n=-\infty}^{\infty} G_n \exp\left(\frac{2\pi i n}{T_{\text{phys}}}(t(k)-t_0)\right). \tag{7}$$

Note the subscript "S" that indicates a function as it appears after sampling. In the context of 3D fMRI, k should be interpreted as the position along the slow k-space axis, usually k_z. Taking the inverse spatial Fourier transform of this expression, we obtain the physiological noise in image space after sampling and reconstruction

$$p_S(z,t_0) = \mathbf{F}^{-1}\{P_S(k,t_0)\}. \tag{8}$$

The time offset t_0 varies according to Eq. (4). It is essential to note the difference between the physiological noise signal $p(z,t,t_0)$, which represents a physical object, and $p_S(z,t_0)$ which is its appearance after sampling and reconstruction. It is only the latter that affects our images. Fig. 2 shows an example of a physiological noise signal, the corresponding oscillating k-space representation, and the reconstructed signal for a Gaussian spatial function $h(z)$.

Vector addition of the static signal with a reconstructed noise component that is in phase with the static signal has a much larger effect on the magnitude of the summed signal than a noise component that is 90° out of phase with the signal. A component that is in phase with the signal will be referred to as *parallel* and a component 90° out of phase as *orthogonal*. The physical noise signal itself can have parallel and orthogonal components and the reconstructed signal can have parallel and orthogonal components. A

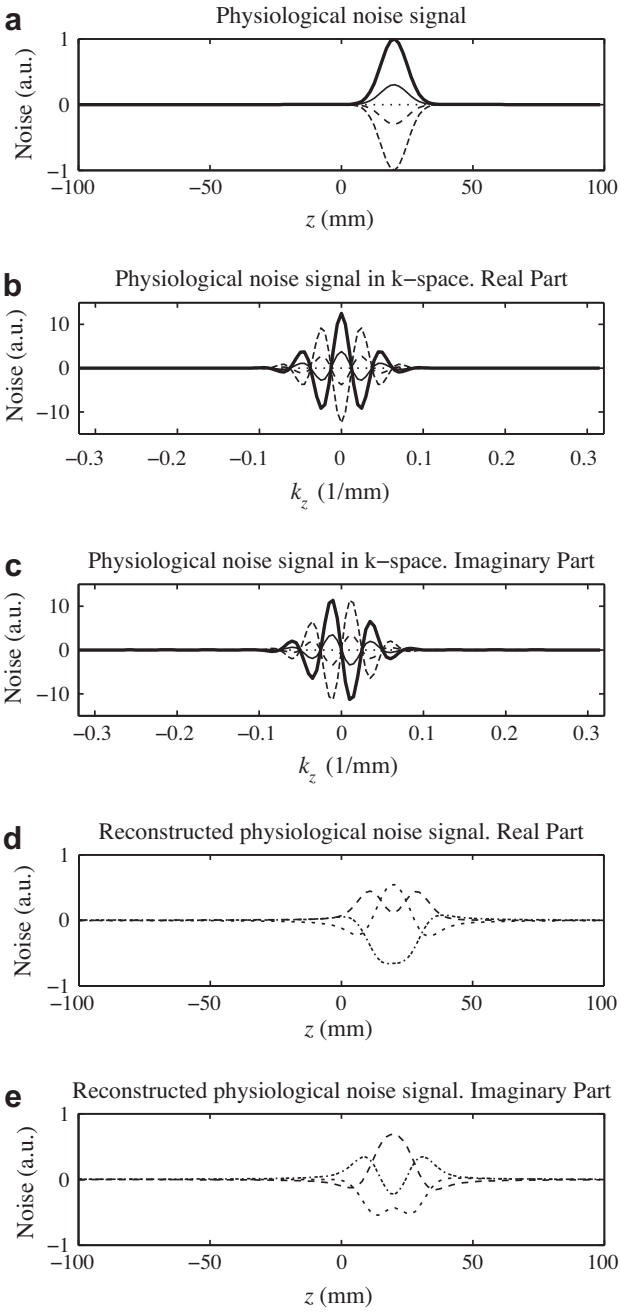

Fig. 2. Physiological noise, the corresponding oscillating k-space representation and the reconstructed physiological noise. (a) The physiological noise signal at five instants in time. The temporal period T_{phys} of this signal is one second, which is a typical value for cardiac noise. The bold line shows the spatial function $h(z)$, which is a Gaussian with unit strength and width 5 mm centered at $z = 20$ mm. (b) and (c) The physiological noise signal in k-space at the same instants in time. The k-space function oscillates with the same period as the physiological noise signal. The bold lines in (b) and (c) show the Fourier transform of $h(z)$. Assuming that the background phase $\varphi(z)$ equals zeros, the signal in (a) is real and the k-space signal possesses conjugate symmetry. (d) and (e) The reconstructed noise signal for four consecutive volumes with volume time $T_{\text{vol}} = 2.24$ s. The sampling scheme is Centric. The period of the reconstructed signal, which is longer than T_{phys}, depends on the ratio $T_{\text{vol}}/T_{\text{phys}}$.

parallel (orthogonal) component in the physical signal does not necessarily translate into a parallel (orthogonal) component in the reconstructed signal. This is explained in the following section. To find the parallel and orthogonal parts of a signal we divide by $\exp[i\varphi(z)]$ and calculate the real and imaginary parts respectively. In the absence of a background phase (i.e. $\varphi(z) = 0$) parallel is

equivalent to real and orthogonal is equivalent to imaginary. If the static signal is much larger than the noise signal, then an orthogonal oscillation will appear approximately as a phase oscillation with little effect on the magnitude.

2.2. Properties of the sampling schemes

We give a short description and motivation for the various sampling schemes. Although we limit the discussion to Cartesian sampling along the slow axis, each k-space plane can be read out with a non-Cartesian scheme, e.g. spiral.

Linear and *Segmented* sampling are the standard ways of traversing k-space. For these sampling schemes we can find analytic expressions for the appearance of the physiological noise in image space after sampling and reconstruction (see Appendix A).

Random, incoherent sampling is considered firstly to examine the effect of noise when coherent noise build-up is being suppressed and secondly because it is the sampling scheme that is effectively implied in compressed sensing. The average behavior in closed form is given in Appendix A.

Centric sampling is considered because it minimizes the parallel component of the reconstructed noise signal p_S if the temporal part $g(t)$ of the physiological noise signal p is imaginary. (The latter requires $G_{-n} = G_n$ with all G_n imaginary or $G_{-n} = -G_n$ with all G_n real in Eq. (5).) For simplicity we assume $\varphi(z) = 0$ and get

$$P(k,t,t_0) = H(k)g(t-t_0). \tag{9}$$

Now, consider the inversion symmetry in k-space. With Centric sampling k and $-k$ are acquired approximately at the same time. Hence, the value of the imaginary temporal function is approximately the same, e.g. $i\gamma$ with γ real. We then have

$$\begin{aligned} P_S(k,t_0) &= i\gamma H(k) \\ P_S(-k,t_0) &= i\gamma H(-k) = i\gamma H^*(k), \end{aligned} \tag{10}$$

where the conjugate symmetry $H(-k) = H^*(k)$ is fulfilled because $h(z)$ is a real function. Eq. (10) implies that $P_S(-k,t_0) = -P_S^*(k,t_0)$, i.e. the k-space associated with the physiological noise possesses conjugate asymmetry. The reconstructed signal from an imaginary noise component is therefore imaginary (i.e. orthogonal, since $\varphi(z) = 0$). Equivalently, if the temporal signal is real, the signal after reconstruction will be real.

Tuned sampling will minimize the parallel component of the reconstructed noise if the temporal part of the physiological noise signal is real and if it satisfies the symmetry requirement

$$g(t + T_{\text{phys}}/2) = -g(t), \tag{11}$$

The data acquisition at k and $-k$ are now separated by $T_{\text{phys}}/2$. Hence we find (still assuming $\varphi(z) = 0$)

$$\begin{aligned} P_S(k,t_0) &= \gamma H(k), \\ P_S(-k,t_0) &= -\gamma H(-k) = -\gamma H^*(k). \end{aligned} \tag{12}$$

This implies that $P_S(-k,t_0) = -P_S^*(k,t_0)$, which means that the real (parallel) physiological noise signal will be rendered imaginary (orthogonal) after sampling and reconstruction. Likewise, an imaginary noise signal will become real in the reconstructed image.

3. Experimental

3.1. Numerical simulations

Physiological noise was simulated numerically. We constructed the sampled k-space and the sampled image using Eqs. (7) and (8) respectively. The Fourier operation was a discrete and finite version of Eq. (13). We used a FOV of 200 mm with matrix 128. The spatial function was a Gaussian with unit strength and width 5 mm centered at $z = 20$ mm (see Fig. 2a). We assumed no spatial phase variation ($\varphi(z) = 0$). The volume acquisition time was $T_{\text{vol}} = 2.24$ s and the period of the physiological noise was $T_{\text{phys}} = 1$ s (corresponding to a heart rate of 60 beats per minute). The time offset t_0 assumed several values in the interval $|0, T_{\text{phys}}\rangle$. We calculated both the real and imaginary parts of the signal, which, since $\varphi(z) = 0$, correspond to the parallel and orthogonal noise components respectively.

3.2. Measurements

The experiments were performed on a Siemens TIM Trio 3T whole-body clinical scanner (Siemens Healthcare, Erlangen, Germany). The subjects were six healthy volunteers (age 27 ± 5 years) whose informed consent was sought and obtained. The experiment was conducted in accordance with the ethical guidelines of our hospital. To focus solely on cardiac effects, the measurements were performed during breath-hold.

We conducted 2D gradient-echo, EPI single-slice measurements with high temporal resolution (70 ms). We acquired 550 frames and calculated both magnitude and phase. These measurements were used to calculate averaged, absolute value noise spectra and to characterize the signal in the complex plane. For four volunteers (no. 1, 2, 3 and 6), we acquired a transversal slice that contained the ventricles and then a slice containing only brain tissue positioned superior to the ventricles. CSF flow out of the slice between excitation and readout was negligible, since the slice thickness divided by the echo time corresponds to a velocity of 0.12 m/s which is much faster than CSF flow. For one volunteer (no. 5), we acquired seven 2D slices. The purpose was to locate the spatial origin of the physiological noise.

We also performed 3D, whole-brain measurements with the sampling schemes discussed in Theory. The 3D sequences were programmed using Siemens' IDEA package. 32 transversal k-space planes were read out with single shot echo-planar acquisition. The readout patterns in the 3D phase encoding ("slow") direction are shown in Fig. 1. The number of segments in the Segmented scheme was $N_{\text{seg}} = 4$. The delay between k and $-k$ in the Tuned scheme was 0.5 s. This matches a cardiac period of 1 s, which corresponds to 60 beats per minute. We conducted measurements with 70 ms spacing between the excitation pulses, giving a volume time of 2240 ms. 16 volumes were recorded. This was done with FH as the slow direction for volunteers no. 1, 2, 3 and 4, and with LR as the slow direction for volunteer no. 2. We also performed measurements with 125 ms spacing between excitation pulses (giving a volume time of 4000 ms) and FH as the slow direction. We then recorded 9 volumes, and performed two runs to improve the statistics. This was done for volunteers no. 2 and 5.

In all measurements, 2D as well as 3D, the voxel size was 3.4 mm isotropic, which is a typical value for gradient echo blood oxygen-level dependent (BOLD) fMRI. The in-plane matrix was 64×64, the read-out bandwidth was 3005 Hz/pixel and the echo time was 27 ms. We employed gradient echo sequences with gradient spoiling for all measurements. The flip angle was 20°. The readout time for one k-space plane was approximately 50 ms. The cardiac-induced physiological noise is frozen out on this time scale, and noise propagates mainly in the slow k-space direction. Hence the problem is effectively one-dimensional.

3.3. Postprocessing

The images were normalized by the thermal noise level, which was estimated from several regions of interest (ROIs) well separated from the object and its ghosts. We suppressed contributions from outside the head by calculating a noise mask that was based on the mean signal intensity in the Linear 3D cube. Voxels with

mean intensity lower than twice the thermal noise level were excluded from the analysis. The five outermost slices on each side in the slow direction were also excluded due to fold-in artifacts. The total temporal variation, *tSD*, was calculated voxelwise as the standard deviation of the voxel intensity along the temporal direction. The first four of the 16 volumes were discarded to ensure steady state conditions. We also calculated the volume fraction that was severely affected by physiological noise, defined as the fraction of voxels with *tSD* higher than 1.5 times the thermal noise level.

4. Results

4.1. Numerical simulations

Fig. 3 shows simulated traces of the reconstructed signal $p_S(z,t_0)$ for all sampling schemes with either parallel or orthogonal harmonic noise. With Random sampling, the reconstructed signal is distributed equally over the entire imaging FOV. This is explained in Appendix A. With Segmented sampling the reconstructed signal is also distributed to parts of the FOV that are well separated from the noise source. This is a ghosting effect that is discussed in mathematical terms in Appendix A. We have only shown results for $N_{seg} = 4$. In general the noise pattern for Segmented sampling is a complicated function of the acquisition parameters. As explained in Theory, Centric sampling suppresses orthogonal noise and Tuned sampling suppresses parallel noise. This behavior is observed in Fig. 3. For Linear sampling with parallel, harmonic noise (as in Fig. 3), Eq. (22) implies that the orthogonal part will vanish when the acquisition matrix, N, is large. With $N = 128$, however, it still has approximately half the strength of the parallel part. The results shown in Fig. 3 were calculated with a background phase equal to zero. We have also carried out

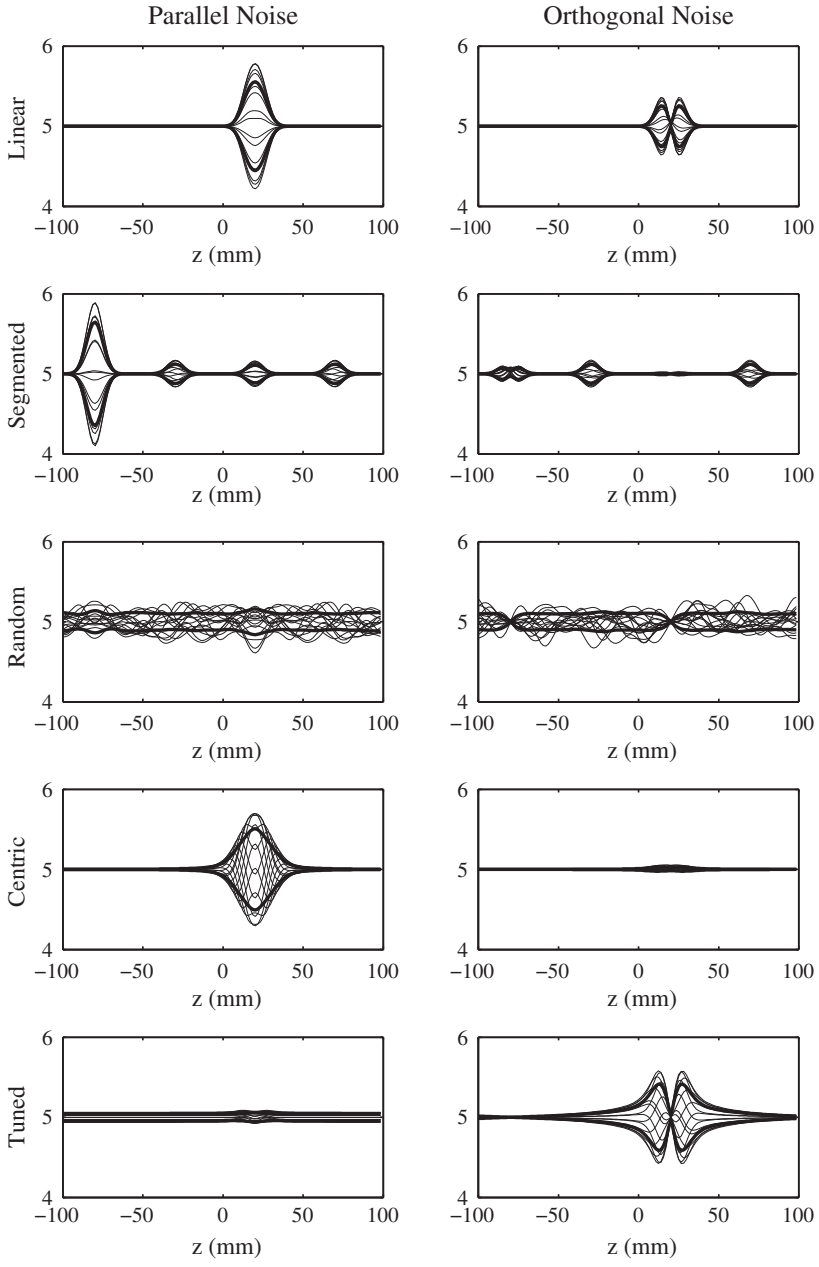

Fig. 3. Simulation results that show traces for different values of t_0 (thin lines) and temporal standard deviation (*tSD*) over all t_0 (bold lines). We show the magnitude of the reconstructed image, assuming a uniform static background signal with intensity 5. Different values of t_0 corresponds to different volumes in a dynamic acquisition. Left: Harmonic noise and parallel oscillation: $G_{-1} = G_1 = 1/2$, while other Fourier components in Eq. (5) equal zero. Right: Orthogonal oscillation ($G_{-1} = G_1 = i/2$).

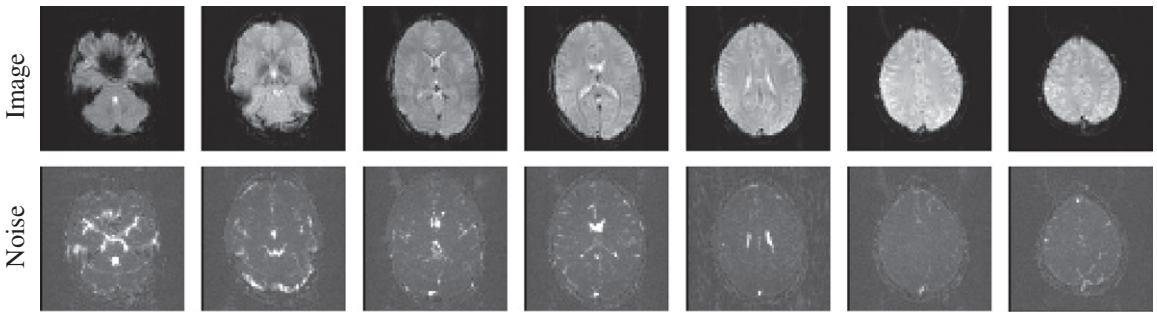

Fig. 4. Sources of physiological noise detected by 2D single slice measurements with high temporal resolution (70 ms). 550 frames were acquired. The first 200 were discarded to ensure steady-state conditions. The lower row (Noise) shows the standard deviation calculated across the remaining frames.

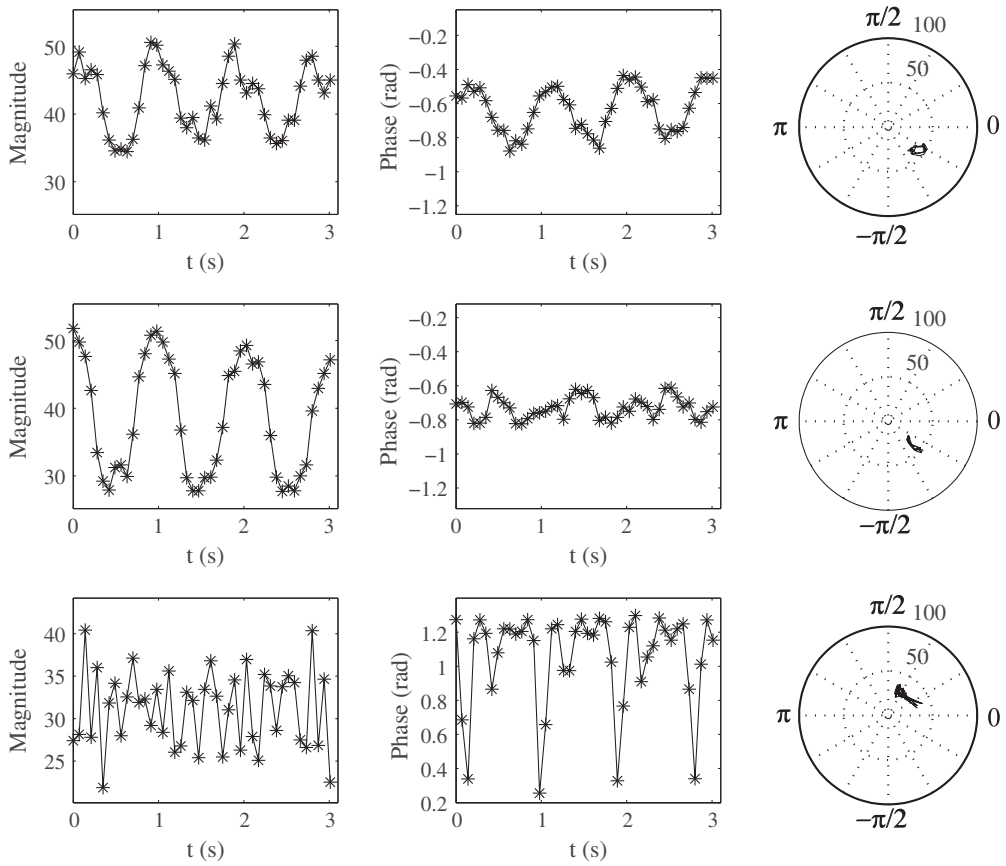

Fig. 5. Magnitude (in units of the thermal noise level) and phase measured in three pixel in the ventricles over a period of 3 s. The rightmost column depicts the signals in the complex plane. Top: Circular oscillation. This corresponds to one single Fourier component in the noise model, Eq. (5). The static background signals is $42e^{-0.75i}$. Middle: Parallel oscillation. The static background signals is $40e^{-0.75i}$. Bottom: Orthogonal oscillation. The static background signals is $31e^{1.15i}$.

simulations with a strong, parabolic phase variation (results not shown). The characteristic behavior of the sampling schemes was not affected.

4.2. Measurements

The results of the 2D high temporal resolution measurements are shown in Figs. 4–6. Fig. 4 shows the spatial origin of the physiological noise. Seven slices, starting in the basal part of the brain and ending superior to the ventricles, are shown. The main sources of noise are found in the basal parts of the brain and in the ventricles. Very little noise is seen superior to the ventricles. Fig. 5 shows the signal measured in three different voxels in the ventricles over a period of 3 s (a typical volume time). The signals are also plotted in the complex plane. We observe examples of both parallel and orthogonal oscillations as well as circular motion, which is a combination of the two pure patterns.

Fig. 6 shows absolute value noise spectra averaged over small ROIs that include only the ventricles for two different subjects. Spectra from ROIs in the slice superior to the ventricles (data not shown) possess a similar pattern of peaks, but the intensity is approximately one order of magnitude lower. This, together with Fig. 4, shows that the ventricles and the basal parts of the brain are the most important sources of cardiac-induced noise. There are large individual variations in the pattern of harmonics in the noise spectra.

The average whole-brain noise levels measured in the 3D experiment are given in Table 1. The noise levels are given in units of the

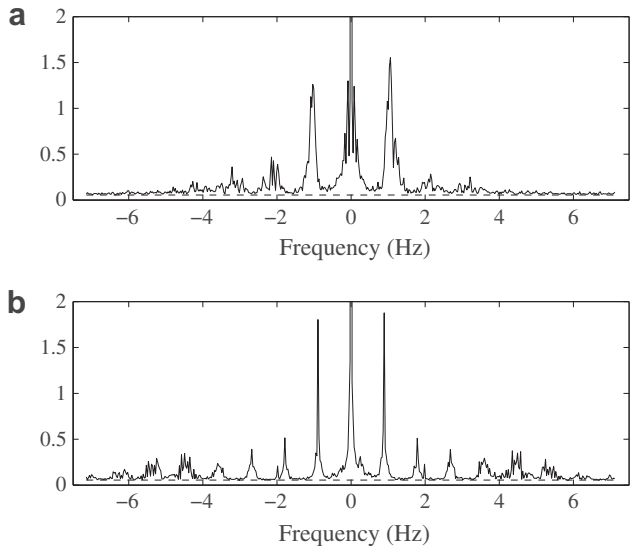

Fig. 6. Averaged noise absolute value spectra from an ROI that covers the ventricles for two different subjects. The dashed line is the Rician noise floor. (a) A spectrum with only a few significant peaks. The temporal noise signal, Eq. (5), can be approximated well by a small number of Fourier components. (b) A spectrum with significant contributions from higher harmonics.

thermal noise. The ratio of signal to thermal noise was approximately 100. The volume fraction of the image with *tSD* higher than 1.5 times the thermal noise level is given in Table 2. Tuned and Linear sampling gives the best results by both criteria, with Centric and Random performing significantly worse.

Fig. 7 shows noise maps for Subject 3. Noise is seen to propagate from the ventricles and the basal parts of the brain into other parts of the volume. Fig. 8 shows the noise level as a function of the position along the slow k-space axis. Random and Centric sampling give high noise levels over the entire volume. Linear sampling has a high noise level near the physical noise sources (ventricles and basal parts of the brain). Segmented sampling propagates the noise to the superior parts of the brain. Tuned sampling gives less noise than Linear near the noise sources, and a comparable noise level in superior brain regions that do not contain physical noise sources. There are large individual variations in the noise level across the subjects. Centric and Random sampling does not perform well neither in ventricles nor in tissue. Segmented sampling performs well in the ventricles but the noise appears at other locations in the volume. This is not a desired feature.

5. Discussion and conclusions

The preferable sampling schemes are Linear and Tuned. Segmented sampling has comparable performance in terms of total noise and noise affected fraction, but the ghosting pattern is unpredictable. Centric and Random sampling yield very poor results.

The signal behavior observed in the 3D measurements is largely consistent with the numerical simulations shown in Fig. 3. The exception is Centric sampling which gives slightly higher noise levels than expected. The noise stems mainly from the ventricles and the basal parts of the brain.

In Fig. 6 we observe well-defined peaks in the noise spectra corresponding to the heartbeat frequency and its harmonics. This suggests that the assumption of a periodic signal is reasonable. However, there are individual differences. In Fig. 6a the peaks are wider than in Fig. 6b. Wider peaks indicate larger deviations from perfect periodicity. Fig. 4 shows that the noise generation is localized to specific regions in the brain. This justifies our choice of a localized spatial function in the numerical simulations.

The model that we have introduced is versatile. Including noise with a different periodicity, such as respiration or quasiperiodic resting brain fluctuations, is trivial. One limiting assumption, however, is separability. If this is not realistic we can introduce space-dependent Fourier components, $G_n(z)$, in Eq. (5). Another refinement is to allow deviations from perfect periodicity. This complicates the analytical treatment, but numerical simulations are still straightforward. Although this paper focuses on brain imaging, the conclusions apply to 3D imaging of any anatomical region that is affected by cardiac-induced physiological noise.

Deviations from perfect periodicity have two effects. Firstly, the evolution of t_0 will be more complicated than stated by Eq. (4), and the succession of reconstructed images will become less predictable. Secondly, the shape of the traces will become somewhat altered (in particular for Segmented sampling). Qualitatively, however, our simulations capture the essential features of the sampling effects.

In this work we have considered a 1D k-space excursion. Some generalizations applicable to a 2D excursion can be drawn. For Random sampling, the generalization is obvious. For Centric sampling, the 2D version amounts to acquiring k and $-k$ as closely as possible in time. Tuned sampling in 2D implies acquiring k and $-k$ with a delay equal to $T_{\text{phys}}/2$. The symmetry properties of Centric and Tuned (discussed in Theory) apply equally well to a 2D k-space excursion. Hence, Centric will still suppress orthogonal noise and Tuned will suppress parallel noise. In the measurements, we employed standard Cartesian EPI without parallel acceleration. Modifications such as spiral acquisition or parallel acceleration of

Table 1
Measured noise (*tSD*) in units of the thermal noise level. Normalized noise is the noise divided by the noise averaged over all schemes for a given subject. This quantity facilitates the comparison and ranking of the schemes.

Subject	T_{vol} (s)	Slow dir.	Noise					Normalized noise				
			Linear	Centric	Segmented	Random	Tuned	Linear	Centric	Segmented	Random	Tuned
1	2.24	FH	1.95	2.39	2.01	2.17	1.81	0.95	1.16	0.97	1.05	0.88
2	2.24	FH	1.50	1.87	1.56	2.01	1.49	0.89	1.11	0.93	1.19	0.88
3	2.24	FH	1.81	2.05	1.66	2.22	1.76	0.95	1.08	0.87	1.17	0.93
4	2.24	FH	1.45	1.69	1.40	1.71	1.39	0.95	1.10	0.91	1.12	0.91
Mean			**1.68**	**2.00**	**1.66**	**2.03**	**1.61**	**0.94**	**1.11**	**0.92**	**1.13**	**0.90**
SD			**0.24**	**0.30**	**0.26**	**0.23**	**0.20**	**0.03**	**0.03**	**0.04**	**0.06**	**0.02**
2	2.24	LR	1.60	1.72	1.58	1.78	1.60	0.97	1.04	0.96	1.07	0.96
2	4.00	FH	1.68	1.59	1.61	1.82	1.76	0.99	0.94	0.95	1.07	1.04
5	4.00	FH	1.77	1.97	1.76	1.78	1.61	1.00	1.11	0.99	1.00	0.90
Mean			**1.73**	**1.78**	**1.69**	**1.80**	**1.69**	**0.99**	**1.02**	**0.97**	**1.04**	**0.97**
SD			**0.06**	**0.27**	**0.10**	**0.03**	**0.11**	**0.00**	**0.12**	**0.03**	**0.05**	**0.10**

Table 2
Noisy volume fraction defined as the fraction of the imaged volume that has a noise level higher than 1.5 times the thermal noise level.

Subject	T_{vol} (s)	Slow dir.	Noisy volume fraction					Normalized noisy volume fraction				
			Linear	Centric	Segmented	Random	Tuned	Linear	Centric	Segmented	Random	Tuned
1	2.24	FH	0.49	0.61	0.52	0.61	0.43	0.92	1.14	0.98	1.15	0.82
2	2.24	FH	0.36	0.51	0.40	0.58	0.35	0.81	1.15	0.90	1.32	0.80
3	2.24	FH	0.47	0.55	0.42	0.63	0.47	0.93	1.08	0.82	1.25	0.92
4	2.24	FH	0.32	0.43	0.29	0.49	0.30	0.87	1.18	0.80	1.33	0.82
Mean			**0.41**	**0.52**	**0.41**	**0.58**	**0.39**	**0.88**	**1.14**	**0.88**	**1.26**	**0.84**
SD			**0.08**	**0.07**	**0.09**	**0.06**	**0.08**	**0.05**	**0.04**	**0.08**	**0.09**	**0.06**
2	2.24	LR	0.35	0.40	0.34	0.47	0.35	0.91	1.05	0.90	1.24	0.91
2	4.00	FH	0.41	0.39	0.40	0.50	0.45	0.96	0.91	0.92	1.17	1.04
5	4.00	FH	0.46	0.54	0.47	0.49	0.40	0.98	1.14	0.99	1.05	0.85
Mean			**0.44**	**0.47**	**0.43**	**0.50**	**0.42**	**0.97**	**1.02**	**0.96**	**1.11**	**0.94**
SD			**0.04**	**0.10**	**0.05**	**0.01**	**0.03**	**0.02**	**0.16**	**0.05**	**0.09**	**0.14**

the acquisition of each k-space plane, does not affect our arguments since the problem remains effectively one-dimensional. Including parallel imaging in the slow k-space direction, however, would require a more complicated model than the present 1D version.

We have shown that it is essential to consider physiological noise when choosing the sampling scheme. Another way to reduce the noise would be to choose the volume time such that the fraction T_{vol}/T_{phys} is approximately integer. Then, according to Eq. (4), the time offset t_0 would not change much from one volume to the next (except for Random sampling, where t_0 is irrelevant). Assuming perfect periodicity, this means that the acquisition of consecutive volumes start at the same instant in the heart cycle, hence giving only minor changes from one volume to the next. The physiological noise would then not be rendered noise-like but rather as a slow signal drift that can be removed by detrending. With ECG-triggering the change from one volume to the next could be kept even smaller. If T_{vol} in the 3D acquisitions were made shorter, the propagation of noise from the ventricles and the basal parts of the brain would be reduced. Imaging techniques that give whole-brain volume times shorter than T_{phys} could be combined with triggering to reduce the physiological noise significantly.

The physiological noise is proportional to the image signal [6]. Therefore, the impact of physiological noise relative to thermal noise can be reduced by acquiring smaller voxels [12]. If high spatial resolution is not needed, one can improve the time-course SNR by acquiring images at high resolution, prior to spatial smoothing [13]. For 3D fMRI sequences that spend all available time between the RF pulses for readout, parallel acceleration reduces the volume time. This reduces the signal intensity, and thereby the ratio of physiological to thermal noise Increased statistical power is then gained due to an increased number of observations within a given time interval. This has been demonstrated for 3D PRESTO (principle of echo shifting with a train of observations) [22] and balanced SSFP (steady-state free precession) [23].

Our simulations (Fig. 3) do not include thermal noise because it would merely appear as a constant offset after averaging. It is interesting, however, to consider the ratio between physiological and thermal noise. Triantafyllou et al. [12] showed that this ratio depended strongly on the field strength. For 3 mm isotropic voxel and 2D imaging the ratio was 0.61, 0.89 and 2.23 at 1.5T, 3T and 7T respectively. For 3D acquisitions, the effect of physiological noise is higher, although suppression of instabilities of the transverse steady-state magnetization by proper RF-spoiling can improve the performance of 3D imaging [24].

Random sampling was shown to yield a very high noise level. This has consequences for compressed sensing where k-space planes are chosen randomly. With a static image the readout order of the randomly chosen k-space lines does not matter. In the presence of physiological noise, however, they should be sorted in ascending or descending order to resemble linear sampling. Another readout strategy that would be efficient in the presence of parallel noise is a hybrid between Tuned and Random sampling, where one half of the k-space positions are chosen randomly and the negative positions are acquired with a delay of $T_{phys}/2$. This would attenuate the physiological noise and, as shown in Appendix A, reduce the spatial correlations.

Tuned sampling may have a potential for reducing physiological noise. In the simulations shown in Fig. 3, however, the noise cancellation is not perfect. A fluctuating DC component persists. The reason is that the central k-space element does not have a conjugate partner. This can be overcome if we read out the central line twice with the required time separation and put in the average of these lines at the center of k-space. We did not implement this in the simulations since it was not implemented in the measurements. In human brain measurements, there are additional factors that limit the noise-cancellation capabilities of the Tuned sampling scheme. Firstly, the physiological noise signal contains orthogonal as well as parallel noise. Secondly, the noise spectra (Fig. 6) may have significant contributions from higher harmonics that will break the required $g(t + T_{phys}/2) = -g(t)$ symmetry. In addition, in this work, we assumed that $T_{phys} = 1$ s for all volunteers. Numerical simulations (not shown) indicate that the method is reasonably robust with respect to variations up to 10%. Improved results might be obtained by adapting the sequence to the individual heart rate. Tuned sampling cannot be expected to work well for arrhythmic patients. In Fig. 1 it is seen that the Tuned sampling scheme has a mismatch in the outer parts of k-space. This is a consequence of the fact that the total number of k-space planes is not divisible by the number of planes in each branch. This does not have serious consequences. In general, for all sampling schemes, it is the readout of the central portion of k-space that is important.

Tuned sampling has a possible application in block-design, high-resolution fMRI. Here the symmetry in Eq. (11) is approximately fulfilled and the signal direction is parallel. In a high resolution acquisition, where the volume time is longer than practical paradigm periods, we could apply Tuned acquisition with a separation time between $-k$ and k equal to half the period of the paradigm. This would render the static object in the parallel part of the reconstructed image and the activation in the orthogonal part. This, however, was beyond the scope of the present paper.

In conclusion, we have suggested a mathematical model to describe physiological noise. We have shown theoretically as well as experimentally that the manifestations of physiological noise depend strongly on the sampling scheme. Noise components that are reconstructed in phase with the signal (parallel) have a much larger effect than components that are reconstructed 90° out of phase (orthogonal). This is a key to understanding the performance

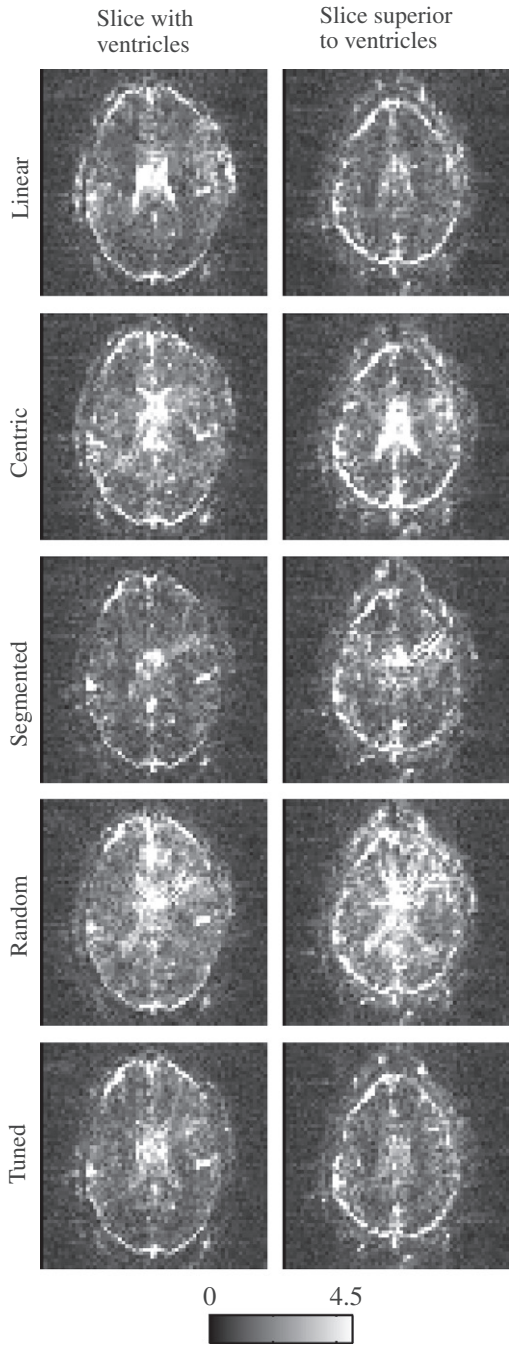

Fig. 7. Noise maps for Subject 3 calculated in a slice that contains the ventricles and a slice superior to the ventricles. The maps are scaled such that the thermal noise level equals unity. The ventricle shaped pattern in the upper slice is noise that has propagated from the source along the slow acquisition direction (feet-head). This mechanism can be observed in the simulations, Fig. 3. It is particularly pronounced for Random sampling.

difference of various sampling schemes. Our analysis indicates that Tuned or Linear acquisition is preferable to Centric, Segmented and Random.

Appendix A

We present some analytic results for the reconstructed physiologic noise signal. We use the symmetric Fourier convention. In continuous form it reads

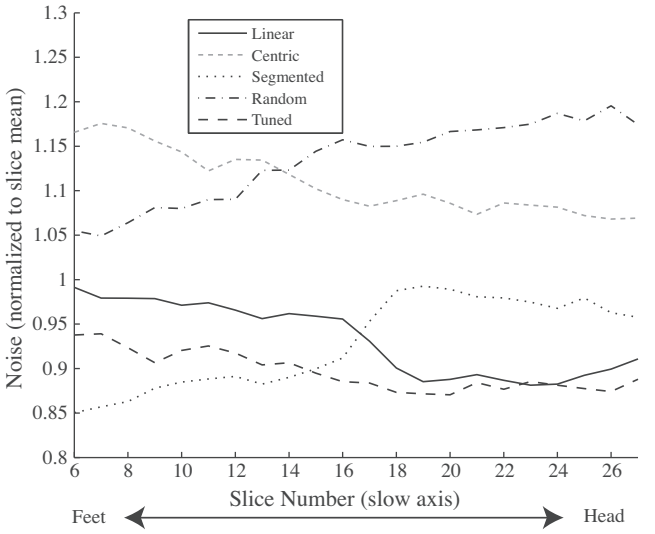

Fig. 8. Noise in reconstructed images as a function of the position along the slow k-space axis (feet-head). The volume time was 2.24 s. The data points are averaged over four volunteers (nos. 1–4). The main physical noise sources are the ventricles and the basal parts of the brain (see Fig. 4). Random and Centric sampling give high noise levels all over. Linear sampling has a high noise level near the physical noise sources. Segmented sampling has a low noise level near the physical sources, but the noise is propagated to the superior parts of the brain. Tuned sampling gives less noise than Linear near the noise sources, and a comparable noise level in the superior parts of the brain. These observations agree with the numerical simulations (Fig. 3).

$$\begin{aligned} H(k) &= \mathbf{F}\{h(z)\} = \int_{-\infty}^{\infty} dz h(z) \mathrm{e}^{-2\pi i k z}, \\ h(z) &= \mathbf{F}^{-1}\{H(k)\} = \int_{-\infty}^{\infty} dk H(k) \mathrm{e}^{2\pi i k z}, \end{aligned} \tag{13}$$

where **F** denotes Fourier transformation. With this definition translations and phase factors have the following effects

$$\begin{aligned} &\mathbf{F}\{h(z)\mathrm{e}^{2\pi i \alpha x}\} = H(k-\alpha), \\ &\mathbf{F}\{h(z-\zeta)\} = \mathrm{e}^{-2\pi i \zeta k} H(k), \\ &\mathbf{F}^{-1}\{H(k)\mathrm{e}^{2\pi i \alpha k}\} = h(z+\alpha), \\ &\mathbf{F}^{-1}\{H(k-\kappa)\} = \mathrm{e}^{2\pi i \kappa z} h(z). \end{aligned} \tag{14}$$

To obtain analytic expressions for the physiological noise, we can assume a simple linear phase variation,

$$\varphi(z) = 2\pi\kappa z, \tag{15}$$

This assumption is adequate for long-scale phase variations that can be linearized over the field of view (FOV). In this case the general expression, Eq. (7), simplifies to

$$P_S(k, t_0) = H(k-\kappa) \sum_{n=-\infty}^{\infty} G_n \exp\left(\frac{2\pi i n}{T_{\mathrm{phys}}}(t(k) - t_0)\right), \tag{16}$$

where $H(k)$ is the Fourier transform of $h(z)$.

A.1. Linear sampling

With Linear sampling the relationship between sampling time and k-space position is given by

$$t(k) = T_{\mathrm{vol}} \frac{L}{N} k, \tag{17}$$

where L is the FOV and N is the number of samples (hence the interval that is spanned in k-space equals N/L). If we introduce

$$\Delta z \equiv L/N \quad \text{and} \quad \zeta \equiv \frac{\Delta z T_{\mathrm{vol}}}{T_{\mathrm{phys}}}, \tag{18}$$

we obtain the following expression for the sampled k-space signal

$$P_S(k,t_0) = H(k-\kappa)\sum_{n=-\infty}^{\infty} G_n \exp(2\pi i n\zeta k)\exp\left(-\frac{2\pi i n}{T_{\text{phys}}}t_0\right). \tag{19}$$

The inverse Fourier transform of this expression gives the physiological noise signal in image space after sampling and reconstruction,

$$p_S(z,t_0) = \sum_{n=-\infty}^{\infty} G_n h(z+n\zeta)\exp[2\pi i\kappa(z+n\zeta)] \times \exp\left(-\frac{2\pi i n}{T_{\text{phys}}}t_0\right). \tag{20}$$

In the Fourier transform we have assumed infinite integration limits. This is an approximation. In Fig. 9 the analytical expression is compared to the numerical result for two values of the matrix size.

As a special case we consider a parallel and harmonic oscillation ($G_n = 0$ for $|n| > 1$), e.g. with $G_{-1} = G_1 = 1/2$) (which yields $g(t) = \cos(2\pi t/T_{\text{phys}})$. We can then calculate the parallel and orthogonal parts of the reconstructed signal as

$$\begin{aligned}
\Re[p_S(z,t_0)/e^{2\pi i\kappa z}] &= \frac{1}{2}[h(z+\zeta)+h(z-\zeta)]\cos[2\pi(t_0/T_{\text{phys}}-\kappa\zeta)] \\
&\approx h(z)\cos[2\pi(t_0/T_{\text{phys}}-\kappa\zeta)], \\
\Im[p_S(z,t_0)/e^{2\pi i\kappa z}] &= -\frac{1}{2}[h(z+\zeta)-h(z-\zeta)]\sin[2\pi(t_0/T_{\text{phys}}-\kappa\zeta)] \\
&\approx -\zeta h'(z)\sin[2\pi(t_0/T_{\text{phys}}-\kappa\zeta)],
\end{aligned} \tag{21}$$

where the approximation is valid if the function h varies slowly on the length scale ζ. Note that the reconstructed physiological noise is split between the parallel and orthogonal parts of the image even if the physiological noise itself is parallel.

If t_0 does not change much from one volume to the next the physiological noise will be manifest as a slow signal drift. If, however, all values of t_0 are equally probable we find parallel and orthogonal temporal standard deviation, *tSD*, given by

$$\begin{aligned}
\Re[tSD(z)/e^{2\pi i\kappa z}] &\approx |h(z)|/\sqrt{2}, \\
\Im[tSD(z)/e^{2\pi i\kappa z}] &\approx \zeta|h'(z)|/\sqrt{2}.
\end{aligned} \tag{22}$$

This equation assumes a parallel and harmonic oscillation. With an orthogonal harmonic oscillation the real and imaginary parts of Eq. (22) are interchanged. As the resolution increases the imaginary part decreases, since $\zeta \propto \Delta z$.

A.2. Segmented sampling

With Segmented sampling we have

$$t_m(k) = \frac{T_{\text{vol}}L}{N_{\text{seg}}N}k + \frac{T_{\text{vol}}}{N_{\text{seg}}}\left(m - \frac{N_{\text{seg}}-1}{2}\right), \quad m = 0,\ldots,N_{seg}-1, \tag{23}$$

where N_{seg} is the number of segments. Each segment can be considered as a Linear, undersampled measurement which corresponds to a reduced FOV

$$\widetilde{L} \equiv L/N_{\text{seg}}. \tag{24}$$

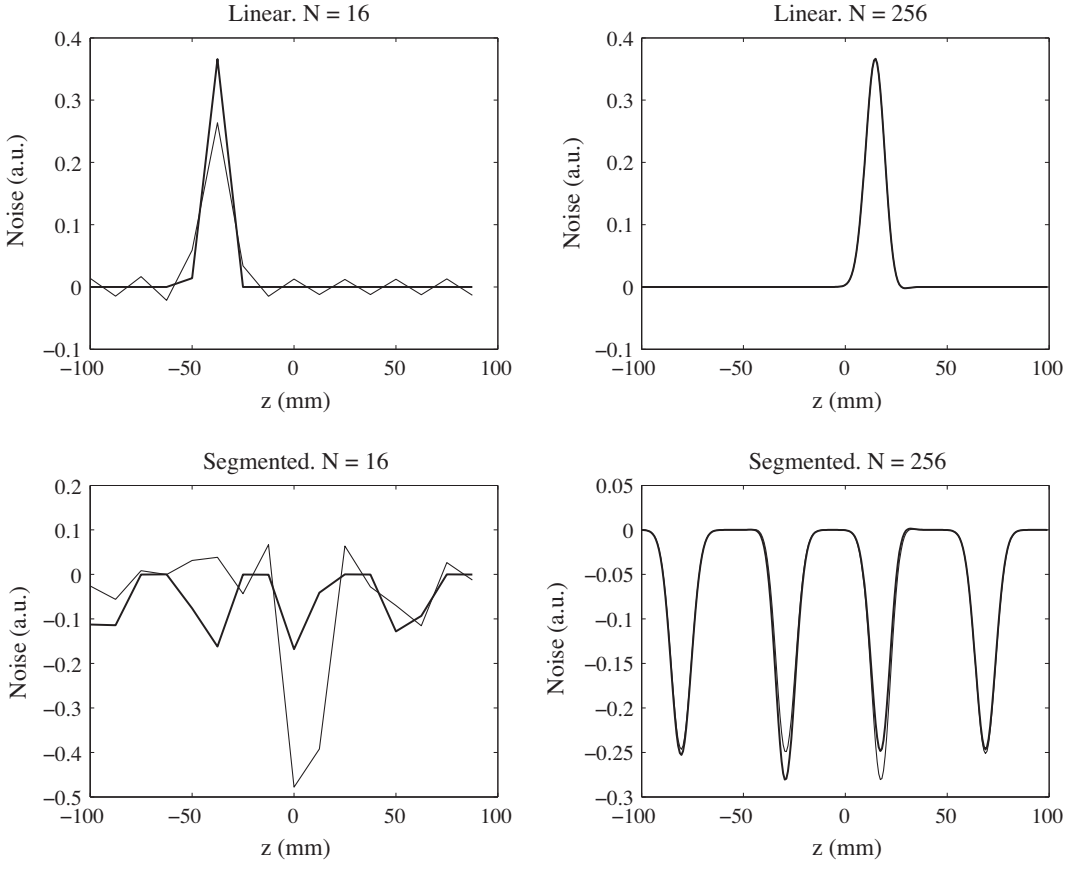

Fig. 9. Finite size effects illustrated with the parallel part of the reconstructed noise signal for Linear and Segmented sampling with $N = 16$ and $N = 256$ samples. Parameters: Fourier component $n = 2$, $t_0 = 0.45$ s, $T_{\text{phys}} = 1$ s, $T_{\text{vol}} = 2.24$ s, $N_{\text{seg}} = 4$ and $\kappa = 1/200$. The Segmented scheme converges more slowly because the N samples are divided between the N_{seg} k-space segments.

To find the total signal we sum the contributions from all segments. We must then implement the fold-in effect that corresponds to the reduced FOV. We must also account for the translation of the sampling grid for the individual segments. In general, if the Fourier transform $F(k)$ of a function $f(z)$ is sampled at a grid with k-space resolution $1/\widetilde{L}$ and with a grid displacement of k_0, then the reconstructed function is given by

$$\sum_{p=-\infty}^{\infty} \exp(2\pi i k_0 \widetilde{L} p) f(z - p\widetilde{L}). \tag{25}$$

This expression is valid for a k-space grid of infinite extension. The k-space displacement for segments m is given by $k_0(m) = m/L$, hence $k_0(m)\widetilde{L} = m/N_{\text{seg}}$. Combining this with Eqs. (20), (23) and (25) we can write

$$\begin{aligned} p_S(z,t_0) &= \frac{1}{N_{\text{seg}}} \sum_{n=-\infty}^{\infty} \sum_{m=0}^{N_{\text{seg}}-1} \sum_{p=-\infty}^{\infty} G_n h(z + n\tilde{\zeta} - p\widetilde{L}) \exp[2\pi i \alpha(n,m,p)], \\ \alpha(n,m,p) &\equiv \kappa(z + n\tilde{\zeta} - p\widetilde{L}) - \frac{n}{T_{\text{phys}}} t_0 \\ &\quad + n\frac{\tilde{\zeta}}{\Delta z}\left(m - \frac{N_{\text{seg}}-1}{2}\right) + mp/N_{\text{seg}}, \\ \tilde{\zeta} &\equiv \zeta/N_{\text{seg}}. \end{aligned} \tag{26}$$

The factor $1/N_{\text{seg}}$ in the sum is a Jacobian. If there is no fold-in in the original image (which was implicitly assumed when we discussed Linear sampling) the summation limits for p should be approximately $\mp N_{\text{seg}}/2$. If we carry out the summation over m we find

$$\begin{aligned} p_S(z,t_0) &= \frac{1}{N_{\text{seg}}} \sum_{n=-\infty}^{\infty} \sum_{p=-\infty}^{\infty} G_n h(z + n\tilde{\zeta} - p\widetilde{L}) \\ &\quad \exp[2\pi i \beta(n,p)] \frac{1 - e^{2\pi i (n\tilde{\zeta}/\Delta z + p/N_{\text{seg}}) N_{\text{seg}}}}{1 - e^{2\pi i (n\tilde{\zeta}/\Delta z + p/N_{\text{seg}})}}, \\ \beta(n,p) &\equiv \kappa(z + n\tilde{\zeta} - p\widetilde{L}) - \frac{n}{T_{\text{phys}}} t_0 \quad - n\frac{\tilde{\zeta}}{\Delta z}\left(\frac{N_{\text{seg}}-1}{2}\right). \end{aligned} \tag{27}$$

The expression for the temporal standard deviation is complicated, but we note that each term in the sum oscillates harmonically as a function of t_0. The parallel and orthogonal parts of the signal are given by $\Re[p_S(z,t_0)/e^{2\pi i \kappa z}]$ and $\Im[p_S(z,t_0)/e^{2\pi i \kappa z}]$ respectively. With Segmented sampling the noise may propagate from the source to the rest of the volume in a complicated manner. Fig. 9 shows the analytical expression and corresponding numerical results.

A.3. Random sampling

For Random sampling analytical solutions cannot be found since the noise signal is rendered in a random manner. We can, however, describe the character of the signal and find its averaged strength. Without loss of generality, we can assume that $\varphi(z) = 0$. Fourier component number n can then be written

$$p^{(n)}(z,t,t_0) \propto \exp\left(2\pi i n \frac{t - t_0}{T_{\text{phys}}}\right) h(z). \tag{28}$$

The k-space representation is

$$P^{(n)}(k,t,t_0) \propto \exp\left(2\pi i n \frac{t - t_0}{T_{\text{phys}}}\right) H(k). \tag{29}$$

Since the k-space positions are acquired at random time points the sampled function, $P_S^{(n)}(K)$, is effectively the product of $H(k)$ and a random phase. The Fourier transform of a random phase vector is a vector of complex Random numbers. This means that the reconstructed signal, $p_S^{(n)}(K)$, will be the convolution of a sequence of random numbers and the function $h(z)$. See Fig. 3 for an example where $h(z)$ is a Gaussian. We see that Random sampling reduces the spatial correlations in the noise.

On average the physiological noise signal is distributed evenly over the FOV and equally between the real and imaginary parts. The temporal standard deviation will be equal to the spatial standard deviation. Hence it can be calculated from

$$\begin{aligned} \Re[tSD]^2 + \Im[tSD]^2 &= \frac{1}{L}\int_{-L/2}^{L/2} dz \left|p_s^{(n)}(z)\right|^2 = \frac{1}{L}\int_{-K/2}^{K/2} dk \left|P_s^{(n)}(k)\right|^2 \\ &= \frac{1}{L}\int_{-K/2}^{K/2} dk |H(k)|^2 = \frac{1}{L}\int_{-L/2}^{L/2} dz h(z)^2, \\ K &\equiv N/L, \quad \text{and} \quad \Re[tSD]^2 = \Im[tSD]^2. \end{aligned} \tag{30}$$

Here we have used the unitarity of the Fourier transform (Parseval's theorem). For simplicity we have expressed the equations in integral rather than summation notation, although Random sampling is only meaningful in the discrete case.

References

[1] S. Lai, G.H. Glover, Three-dimensional spiral fMRI technique: a comparison with 2D spiral acquisition, Magn. Reson. Med. 39 (1998) 68–78.
[2] B.A. Poser, P.J. Koopmans, T. Witzel, L.L. Wald, M. Barth, Three dimensional echo-planar imaging at 7 Tesla, Neuroimage 51 (2010) 261–266.
[3] A. Oppelt, R. Graumann, H. Barfuss, H. Fischer, W. Hartl, W. Schajor, Fast imaging with steady precession – a new fast magnetic resonance imaging sequence, Electromedica (Engl. Ed.) 54 (1986) 15–18.
[4] G. Liu, G. Sobering, J. Duyn, C.T. Moonen, A functional MRI technique combining principles of echo-shifting with a train of observations (PRESTO), Magn. Reson. Med. 30 (1993) 764–768.
[5] M. Lustig, D. Donoho, J.M. Pauly, Sparse MRI: The application of compressed sensing for rapid MR imaging, Magn. Reson. Med. 58 (2007) 1182–1195.
[6] G. Kruger, G.H. Glover, Physiological noise in oxygenation-sensitive magnetic resonance imaging, Magn. Reson. Med. 46 (2001) 631–637.
[7] G. Kruger, A. Kastrup, G.H. Glover, Neuroimaging at 1.5 T and 3.0 T: comparison of oxygenation-sensitive magnetic resonance imaging, Magn. Reson. Med. 45 (2001) 595–604.
[8] X. Hu, T.H. Le, T. Parrish, P. Erhard, Retrospective estimation and correction of physiological fluctuation in functional MRI, Magn. Reson. Med. 34 (1995) 201–212.
[9] B. Biswal, F.Z. Yetkin, V.M. Haughton, J.S. Hyde, Functional connectivity in the motor cortex of resting human brain using echo-planar MRI, Magn Reson. Med. 34 (1995) 537–541.
[10] J. Pfeuffer, P.F. Van de Moortele, K. Ugurbil, X. Hu, G.H. Glover, Correction of physiologically induced global off-resonance effects in dynamic echo-planar and spiral functional imaging, Magn. Reson. Med. 47 (2002) 344–353.
[11] P. van Gelderen, J.A. de Zwart, P. Starewicz, R.S. Hinks, J.H. Duyn, Real-time shimming to compensate for respiration-induced B0 fluctuations, Magn. Reson. Med. 57 (2007) 362–368.
[12] C. Triantafyllou, R.D. Hoge, G. Krueger, C.J. Wiggins, A. Potthast, G.C. Wiggins, L.L. Wald, Comparison of physiological noise at 1.5 T, 3 T and 7 T and optimization of fMRI acquisition parameters, Neuroimage 26 (2005) 243–250.
[13] C. Triantafyllou, R.D. Hoge, L.L. Wald, Effect of spatial smoothing on physiological noise in high-resolution fMRI, Neuroimage 32 (2006) 551–557.
[14] J. Bodurka, F. Ye, N. Petridou, K. Murphy, P.A. Bandettini, Mapping the MRI voxel volume in which thermal noise matches physiological noise-implications for fMRI, Neuroimage 34 (2007) 542–549.
[15] K. Murphy, J. Bodurka, P.A. Bandettini, How long to scan? The relationship between fMRI temporal signal to noise ratio and necessary scan duration, Neuroimage 34 (2007) 565–574.
[16] G.H. Glover, T.Q. Li, D. Ress, Image-based method for retrospective correction of physiological motion effects in fMRI: RETROICOR, Magn. Reson. Med. 44 (2000) 162–167.
[17] M. Bianciardi, M. Fukunaga, P. van Gelderen, S.G. Horovitz, J.A. de Zwart, K. Shmueli, J.H. Duyn, Sources of functional magnetic resonance imaging signal fluctuations in the human brain at rest: a 7 T study, Magn. Reson. Imaging 27 (2009) 1019–1029.
[18] C. Chang, J.P. Cunningham, G.H. Glover, Influence of heart rate on the BOLD signal: the cardiac response function, Neuroimage 44 (2009) 857–869.
[19] M.S. Dagli, J.E. Ingeholm, J.V. Haxby, Localization of cardiac-induced signal change in fMRI, Neuroimage 9 (1999) 407–415.
[20] G.E. Hagberg, M. Bianciardi, V. Brainovich, A.M. Cassara, B. Maraviglia, The effect of physiological noise in phase functional magnetic resonance imaging: from blood oxygen level-dependent effects to direct detection of neuronal currents, Magn. Reson. Imaging 26 (2008) 1026–1040.

[21] N. Petridou, A. Schafer, P. Gowland, R. Bowtell, Phase vs. magnitude information in functional magnetic resonance imaging time series: toward understanding the noise, Magn. Reson. Imaging 27 (2009) 1046–1057.
[22] S.F. Neggers, E.J. Hermans, N.F. Ramsey, Enhanced sensitivity with fast three-dimensional blood-oxygen-level-dependent functional MRI: comparison of SENSE-PRESTO and 2D-EPI at 3 T, NMR Biomed. 21 (2008) 663–676.
[23] M. Chappell, A.K. Haberg, A. Kristoffersen, Balanced steady-state free precession with parallel imaging gives distortion-free fMRI with high temporal resolution, Magn. Reson. Imaging 29 (2011) 1–8.
[24] U. Goerke, H.E. Moller, D.G. Norris, C. Schwarzbauer, A comparison of signal instability in 2D and 3D EPI resting-state fMRI, NMR Biomed. 18 (2005) 534–542.